RSC Advances

RSC Publishing

PAPER

View Article Online
View Journal | View Issue

Cite this: *RSC Advances*, 2013, **3**, 9330

Understanding the photoelectrochemical properties of a reduced graphene oxide–WO_3 heterojunction photoanode for efficient solar-light-driven overall water splitting†

Jingdong Lin,[ab] Peng Hu,[c] Yan Zhang,[a] Meiting Fan,[b] Ziming He,[a] Chee Keong Ngaw,[a] Joachim Say Chye Loo,*[c] Daiwei Liao[b] and Timothy Thatt Yang Tan*[a]

Received 31st January 2013,
Accepted 3rd April 2013

DOI: 10.1039/c3ra40550h

www.rsc.org/advances

WO_3–reduced graphene oxide (WO_3–RGO) heterojunction electrodes were prepared for photoelectrochemical (PEC) overall water splitting. The WO_3 photoanode incorporated with RGO showed significantly enhanced PEC properties and, hence, photocatalytic water splitting, compared to the bare WO_3 at a bias larger than 0.7 V *vs.* Ag/AgCl, while a decrease in the PEC properties of WO_3–RGO compared to the WO_3 electrode was observed at a bias smaller than 0.7 V *vs.* Ag/AgCl. RGO could play a favorable role in enhancing the electron–hole separation due to the presence of interface states according to the Bardeen model, but it could also provide active sites for the electron–hole recombination. A more positive applied bias is in favor of effective electron–hole separation, by means of quick collection and transport of electrons by RGO. As a result, a higher PEC performance of WO_3–RGO can only be realised at a relatively more positive bias. This study gives insights into the complex nature of a RGO–semiconductor heterojunction, and its implications on the overall photoconversion efficiency.

Introduction

Fabrication of photocatalysts with an excellent photo-adsorption ability within the solar spectrum and low recombination rate of photogenerated electron–hole is one of the key requirements for efficient solar hydrogen generation *via* semiconductor photocatalytic overall water splitting.[1–3] Significant effort has been devoted to achieve this goal, for example through the utilization of co-catalysts, doping, Z-scheme photocatalysis, and dye sensitization *etc.*[4–9] Among them, semiconductor incorporation with graphene has attracted considerable interest due to its ability to enhance the mobility of charge carriers and its high specific surface area *etc.*[10–12]

Many different types of graphene–semiconductor composites, such as TiO_2–graphene, CdS–graphene, $Zn_xCd_{1-x}S$–graphene, WO_3–graphene *etc.*, for water splitting have been reported.[13–18] It is generally accepted that graphene mainly plays a favorable role in the electron–hole separation and the quick transport of photogenerated electrons due to the remarkable conductivity of graphene.[19,20] In the case of the semiconductor, WO_3 not only has stronger adsorption within the solar spectrum than TiO_2, but also has a longer hole diffusion length (~150 nm) as compared with Fe_2O_3 (2–4 nm) and TiO_2 (~10 nm), which is in favor of the separation of photogenerated electron–hole.[21–23] Therefore, WO_3 has attracted considerable interest in photocatalytic water splitting. The potential of the WO_3 conduction band (CB) is more positive than that of H^+/H_2.[24] Hence, to achieve an overall water splitting, a photoelectrochemical (PEC) system with a WO_3 photoanode is utilized for the photocatalytic overall water splitting, rather than a suspension reaction system. The thickness of the WO_3 electrode film in the PEC is generally at the micrometer scale,[24] *i.e.* there would be dozens of WO_3 particles in the direction of the film thickness. In this case, the transport of electrons generated by the outer layer WO_3 particles to the substrate is not efficient because of the occurrence of electron–hole recombination at the particle interface. Therefore, quick capture followed by effective transport of electrons to the substrate is necessary for efficient water splitting by the PEC system. Incorporation with RGO is expected to lower the electron–hole recombination in the WO_3 films.

[a]*Solar Fuel Lab, School of Chemical and Biomedical Engineering, Nanyang Technological University, 637459, Singapore. E-mail: tytan@ntu.edu.sg; Fax: (+)65 6794 7553; Tel: (+) 65 6316 8829*

[b]*Department of Chemistry, College of Chemistry and Chemical Engineering, Xiamen University, Xiamen, 361005, China*

[c]*Solar Fuel Lab, School of Materials Science and Engineering, Nanyang Technological University, 639798, Singapore. E-mail: joachimloo@ntu.edu.sg*

† Electronic supplementary information (ESI) available: Experimental details, characterizations and supporting figures. See DOI: 10.1039/c3ra40550h

WO_3–RGO composites have been reported for sensors, photo-degradation, oxygen evolution using a suspension reaction system and PEC studies.[15,25–28] The RGO in WO_3–RGO provides high surface contact, which helps to enhance the charge carriers' extraction and transfer, such as those observed in TiO_2–RGO.[15,24,27] Very few groups have attempted in-depth studies of the role of RGO in WO_3–RGO for light harvesting. Understanding the role of RGO in the WO_3–RGO composites for the PEC overall water splitting would provide further insight into the heterojunction nature of RGO–semiconductor photocatalysts, which has further implications to the wider PEC and photocatalytic applications of RGO heterojunctions. Herein, we report, for the first time, a WO_3–RGO photoanode applied in PEC overall water splitting. The role of RGO in the WO_3–RGO photoanode in solar light harvesting is hereby discussed.

Results and discussion

WO_3–RGO composites were prepared using graphene oxide (GO) as a precursor of RGO, ammonium metatungstate hydrate (AMT) as a precursor of WO_3, and poly vinyl pyrrolidone (PVP) as an intermediate to combine tungsten with GO. The detailed preparation and characterizations can be found in the Supporting Information (ESI†). Field emission scanning electron microscopy (FESEM) images of both the top and cross-section views of WO_3 and the WO_3–RGO electrodes are shown in Fig. 1. The thickness of both films is approximately 1.6 μm as seen from the cross-sectional view. The top view clearly shows a uniform WO_3–RGO film on FTO. Fig. 1 also shows that the WO_3–RGO electrode consists of a more porous structure than that of WO_3. The WO_3 and WO_3–RGO samples have specific surface areas of 13.7 $m^2\ g^{-1}$ and 31.7 $m^2\ g^{-1}$ according to Brunauer–Emmett–Teller (BET) analysis, respectively (see Fig. S5, ESI†). The increase of the specific surface area in the presence of RGO is attributed to the special ordered two-dimensional honeycomb lattice structure of RGO, which is in favor of the uniform distribution of WO_3. Similar results were also reported for TiO_2–RGO composites, which are in favour of high photocatalytic performance.[29]

From the low-resolution transmission electron microscopy (TEM) images (see Fig. S6, ESI†), WO_3 particles of ~20–40 nm in size are observed both over WO_3 and the WO_3–RGO composite. Fig. 2 shows the typical XRD patterns of the prepared WO_3–RGO and WO_3 electrodes calcined at 450 °C. Both hexagonal (JCPDS No. 00-033-1387) and monoclinic (JCPDS No. 01-083-0951) phases were detected. Li *et al.* reported that the mixed phase structure of the WO_3 catalyst was advantageous for enhancing the photo-catalytic performance.[30] No peak at $2\theta \sim 23°$, assigned to RGO, is observed due to the low RGO concentration and the overlapping of the peaks ascribed to WO_3. The structures of WO_3 and the WO_3–RGO nanocomposite were further characterized by high resolution transmission electron microscopy (HRTEM). The HRTEM images (Fig. 2b and 2c) reveal the highly crystalline features of the WO_3 nanoparticles. The fringes with lattice spacing of 0.316, 0.391 and 0.385 nm can be indexed to the (200) and (001) planes of hexagonal WO_3 (JCPDF 00-033-1387) and the (002) plane of monoclinic WO_3 (JCPDF 01-083-0951), respectively, which are consistent with the XRD assignment. The FESEM, TEM and Raman (see Fig. S7, ESI†) results indicate that the WO_3 nanocrystallites were uniformly distributed on the RGO, and a uniform WO_3–RGO electrode was successfully fabricated.

The photocatalytic activities of the WO_3 and WO_3–RGO electrodes were evaluated by measuring the H_2 and O_2 evolution from an overall water splitting PEC system. Fig. 3a and 3b show the H_2 and O_2 evolution–time plots for the WO_3–RGO and WO_3 electrodes at 1 V *vs.* Ag/AgCl under AM1.5 illumination in 0.5 M H_2SO_4 electrolyte, respectively. The WO_3–RGO electrode generates 60 and 27 μmol cm^{-2} of H_2 and O_2 after 4 h, respectively, which are ~2.4 times higher than those of WO_3 (25 and 12 μmol cm^{-2} of H_2 and O_2 after 4 h, respectively). Fig. 3c shows the photocurrent–time plots for the WO_3–RGO photoanode compared with WO_3 under chopped AM1.5 illumination in 0.5 M H_2SO_4 at 1.0 V *vs.* Ag/AgCl. The photocurrent density of the WO_3–RGO electrode is ~1.1 mA cm^{-2}, which is about 2.5 times higher than that of the WO_3 (~0.4 mA cm^{-2}). Several studies on the WO_3–RGO nanocomposites for photocatalytic oxygen evolution using a suspension reaction system and photodegradation have been reported.[15,26] However, to the best of our knowledge and until now, only one work has reported the use of WO_3–RGO for a

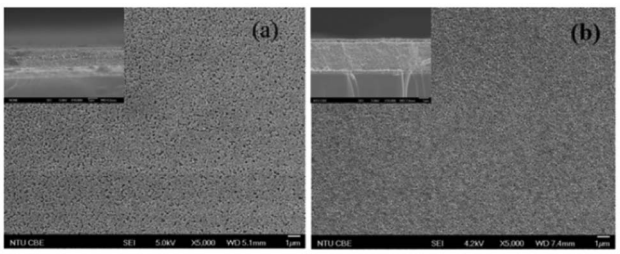

Fig. 1 FESEM images of electrodes, (a) WO_3–RGO; (b) WO_3. (Inset: cross-section of the electrodes)

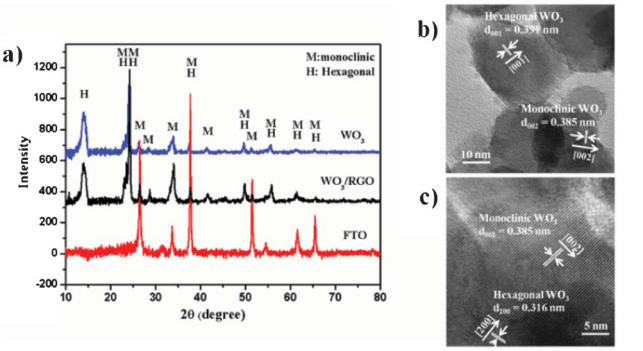

Fig. 2 (a) XRD patterns of electrodes; (b) HRTEM image of WO_3–RGO; (c) HRTEM image of WO_3.

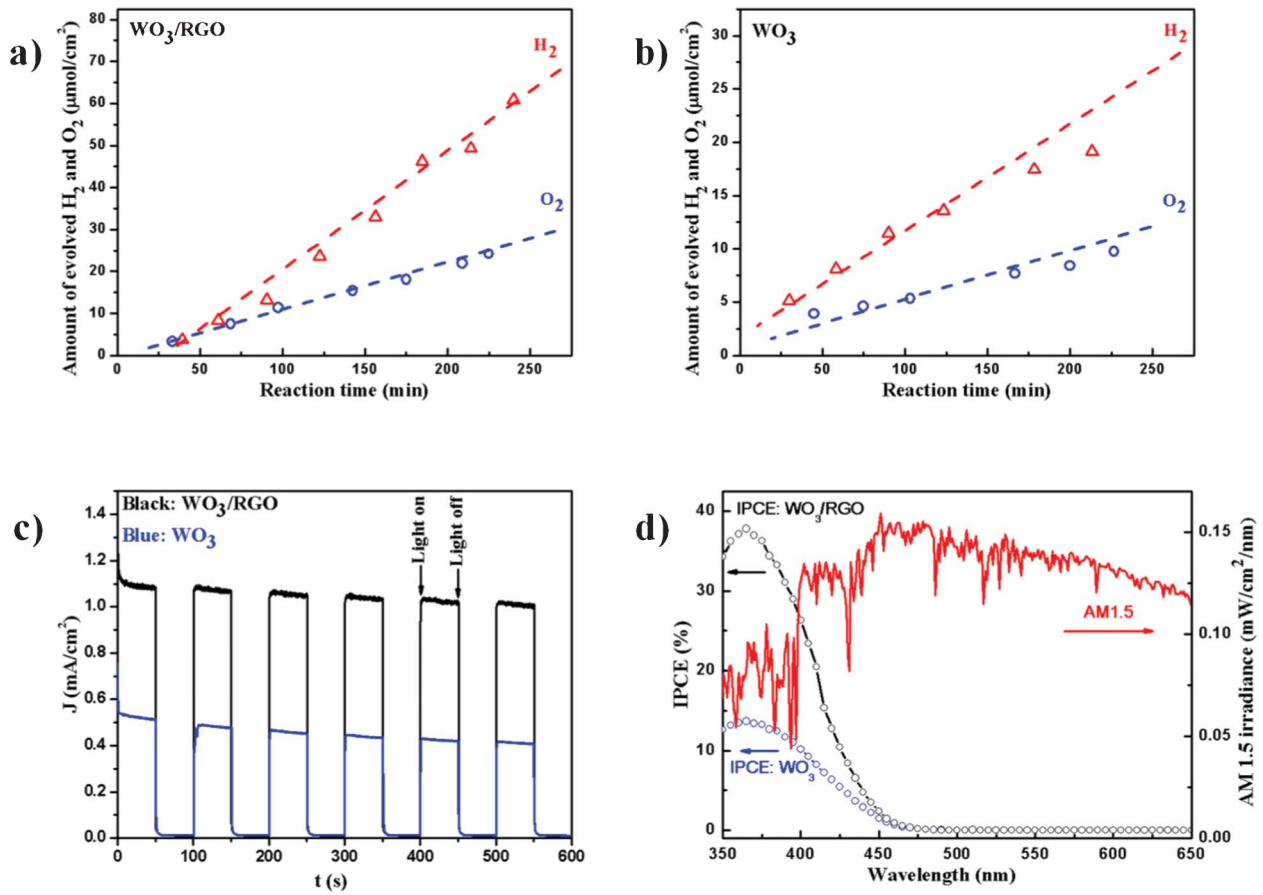

Fig. 3 Evolution of H_2 and O_2 over (a) WO_3–RGO and (b) WO_3 electrodes; (c) chopped photocurrent profiles of WO_3 and WO_3–RGO electrodes; (d) IPCE of WO_3 and WO_3–RGO electrodes. (1.0 V *vs.* Ag/AgCl in 0.5 M H_2SO_4, AM1.5, 100 mW cm^{-2})

PEC study.[28] The application of WO_3–RGO for PEC overall water splitting has not been reported. Though it is difficult to compare the PEC performances due to the different test conditions and preparation methods, we found that the current WO_3–RGO electrode illuminated at 0.75 V in 0.5 M H_2SO_4 (Fig. 4) manifested a current density of about 0.5 mA cm^{-2}, compared to a 20 μA cm^{-2} density from 5% RGO in the WO_3 electrode, fabricated using a drop-cast method under visible light illumination at 0.75 V in 0.1 M Na_2SO_4.[28] The applied bias photon-to-current efficiency (ABPE) was also determined and is shown in Fig. S8, in the ESI.†

Fig. 3d shows the incident photon to electron conversion efficiency (IPCE) curves for the WO_3 and WO_3–RGO electrodes. The IPCE curves for WO_3 and WO_3–RGO have a similar shape. It clearly shows that the photo response of the WO_3 and WO_3–RGO electrodes only occurs at a wavelength less than 500 nm. The IPCE for WO_3–RGO at 1 V *vs.* Ag/AgCl shows a maximum efficiency of about 38% at a wavelength of 360 nm, which is about 2.7 times higher than that of WO_3 (14%). The calculated photocurrents using the IPCE (λ) data shown in Fig. 3d are 1.09 and 0.35 mA cm^{-2} for WO_3–RGO and WO_3, respectively, which are close to the measured photocurrents shown in Fig. 3c.

Both the photocatalytic activities and IPCE results show that the WO_3 photoanode with RGO harvests solar light more effectively than that without RGO, at 1.0 V *vs.* Ag/AgCl. In order to gain further insight into the role of RGO in the WO_3 photoanode, linear sweep voltammetry (LSV), ultraviolet-visible diffuse reflection spectroscopy (UV-Vis/DRS) and electrochemical impedance spectroscopy (EIS) characterizations were carried out. Fig. 4 shows LSV under chopped AM1.5 illumination in 0.5 M H_2SO_4 electrolyte. The onset potential of the photocurrent for the WO_3 electrode appears at ~0.3 V *vs.* Ag/AgCl and continues to increase to ~0.4 mA cm^{-2} at 1.0 V *vs.* Ag/AgCl. In comparison to WO_3, the WO_3–RGO electrode shows a significant enhancement in photoresponse with a photocurrent density of ~1.1 mA cm^{-2} at 1.0 V *vs.* Ag/AgCl. There is no saturation of the photocurrent observed in WO_3–RGO at more positive potential, which indicates an efficient charge separation in WO_3–RGO, under illumination. However, the photocurrent of WO_3 is nearly constant at a bias larger than 0.7 V *vs.* Ag/AgCl, which implies that the overall photoreaction is limited by the charge separation in the WO_3 electrode, under illumination. It is worth noting that the photocurrent density of WO_3 is higher than that of WO_3–RGO at a bias less than 0.7 V *vs.* Ag/AgCl. However, the photocurrent

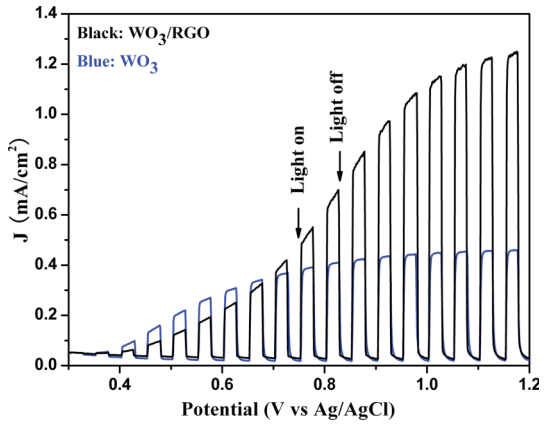

Fig. 4 LSV of the WO_3 and WO_3–RGO electrodes in 0.5 M H_2SO_4, using a scan rate of 5 mV s^{-1} (chopped AM1.5 illumination, 100 mW cm^{-2}).

density of WO_3–RGO exceeds that of WO_3 at a bias larger than 0.7 V *vs.* Ag/AgCl. The results indicate that the presence of RGO in WO_3–RGO can harvest solar light more effectively only at a bias larger than 0.7 V *vs.* Ag/AgCl.

The energy band structures of WO_3 and the WO_3–RGO composite were studied using UV-Vis/DRS. As shown in Fig. 5a, a strong absorption below 500 nm for WO_3 and the WO_3–RGO composite is attributed to the absorption edge of WO_3. The band gap (E_g) obtained using the UV-Vis/DRS data is ~2.55 eV for both WO_3 and WO_3–RGO, which corresponds to the IPCE results (see Fig. S9, ESI†). The small amount of 1% RGO has a negligible effect on the light absorption of WO_3 due to the low concentration of RGO. IPCE is the product of light absorption and carrier collection. Therefore, the UV-Vis/DRS and IPCE results imply that the presence of RGO plays an important role in enhancing the efficiency of carrier collection and transport at a bias of 1.0 V *vs.* Ag/AgCl.

EIS measurements were carried out to understand the intrinsic electronic and charge-transfer properties of WO_3–RGO and WO_3. Fig. 5b and 5c show the Nyquist plots of WO_3 and WO_3–RGO at 0.4 V and 1.0 V *vs.* Ag/AgCl, respectively. The semicircle in the medium-frequency region is assigned to the charge-transfer limiting process.[20,31] When a bias of 0.4 V *vs.* Ag/AgCl is applied, the diameter of the semicircle of WO_3–RGO is larger than that of WO_3 (see Fig. 5b), indicating that the

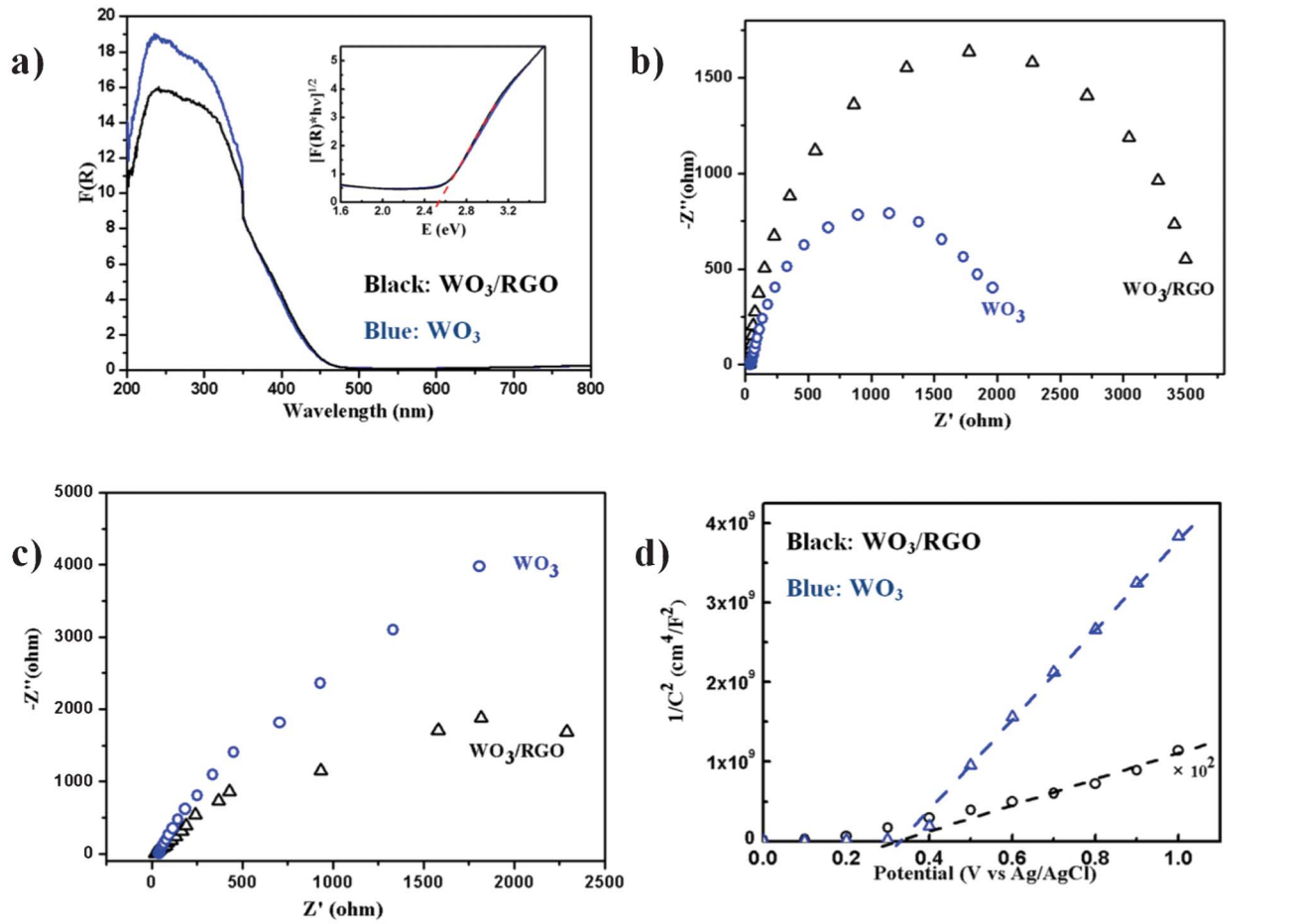

Fig. 5 (a) UV-Vis/DRS spectra of WO_3 and WO_3–RGO (inset shows the Tauc plots calculated from the data). Nyquist plots of WO_3 and WO_3–RGO under AM1.5 illumination in 0.5 M H_2SO_4 at different bias, (b) 0.4 V *vs.* Ag/AgCl; (c) 1.0 V *vs.* Ag/AgCl. (d) Mott–Schottky plots of WO_3 and WO_3–RGO in 0.5 M H_2SO_4 at 1 kHz under AM1.5 illumination.

presence of RGO in the WO_3–RGO film impedes charge transfer. However, at a bias of 1.0 V *vs.* Ag/AgCl, the diameter of the semicircle of the WO_3–RGO film is obviously less than that of WO_3, indicating that RGO in the WO_3–RGO film accelerates the electron transfer. The EIS results show that RGO decreases the electron–hole recombination rate only at a relatively high bias. From the similar trends observed in the characterization results of the photocurrent and recombination rate of electron–hole changing with bias, it can be inferred that efficient electron–hole separation in the presence of RGO is the main reason for the enhancement of photocatalytic activity at a high bias.

As shown in Fig. 5d, the potential of flat bands (U_{fb}) is ~0.3 V *vs.* Ag/AgCl for both the WO_3 and WO_3–RGO electrodes, which is quite close to the onset potential given in Fig. 4. The positive CB potential of WO_3 and WO_3–RGO is below the H^+/H_2 potential. Therefore, even with illumination, H_2 cannot be evolved without external bias. For the H_2 evolution, an external anodic bias (E_{Bias}) is required to raise the Fermi level in the counter electrode above the H^+/H_2 potential.[32] When the bias is more positive than the onset potential, the photogenerated electrons in CB are collected by the substrate to form an external circuit and H_2 is generated at the Pt electrode, with the corresponding O_2 generated at the WO_3 electrode. Therefore, the efficiency of electron transport and collection in WO_3 film is a critical factor in determining the overall photocatalytic performance.

To better understand how the interaction of RGO and WO_3 could affect the electron–hole separation, the energy band structures of RGO and WO_3 in WO_3–RGO should be considered. It is well known that GO will undergo insulator–semiconductor–semimetal transitions in the process of thermal reduction to RGO.[33] The apparent transport gap of RGO approaches zero with extensive reduction.[33] Therefore, RGO can be regarded as a kind of metal-like material with work function of 4.61 to 4.71 eV.[33–35] The change of the energy band structure of RGO and WO_3 in WO_3–RGO can be explained by the classic metal–semiconductor contact theory. If the work function of the metal is higher than that of the semiconductor, a Schottky barrier is formed between the metal and semiconductor. The photogenerated electrons in the CB of the semiconductor can be collected by the metal under illumination to reduce the recombination of the electron–hole due to the Schottky barrier. For example, the work function of RGO is 4.61 to 4.71 eV, which is larger than that of TiO_2 or CdS.[13,14,33] When the RGO is incorporated with TiO_2 or CdS, the photogenerated electrons in the CB of TiO_2 or CdS can be easily transferred to RGO under illumination due to the difference in the work function. The good photocatalytic performance of the TiO_2–RGO or CdS–RGO composites is

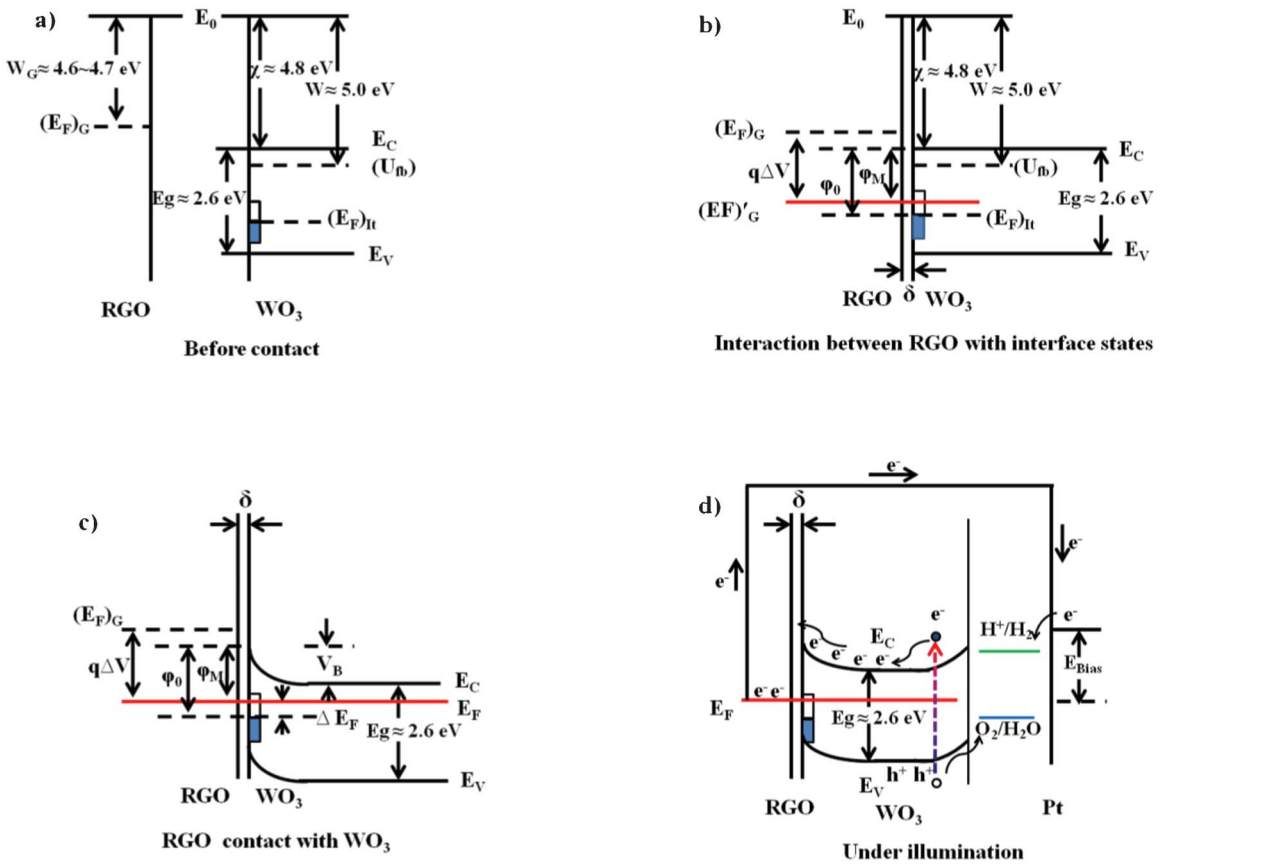

Scheme 1 Sequence of energy level diagrams for RGO contacted with WO_3.

generally ascribed to the improved electron collection and fast transport by the RGO.[13,14] However, electrons in the CB of WO_3 cannot be injected to the RGO due to the lower work function of RGO compared with WO_3, taking energy levels into account. However, interface states are readily formed in composites, such as graphene and semiconductor composites *etc.*[35,36] In this case, the Schottky barrier can be formed with the help of the interface states based on the Bardeen model as shown in Scheme 1.[37,38] We first assume that RGO interacts with the interface states for the sake of simplicity. When the WO_3–RGO composite is formed initially, the free electrons are transferred from the RGO to the interface states due to the lower Fermi level of the interface states ($(E_F)_{it}$) compared with the RGO ($(E_F)_G$), until an equilibrium is achieved ($(E_F)_G$ drops and $(E_F)_{it}$ rises), which results in equal Fermi levels for RGO and interface states. The difference of the Fermi level of RGO due to the interaction of RGO and the interface states, $q\Delta V$, is about 1 eV in scale, generally.[38] Therefore, the Fermi level of RGO and interface states is lower than that of WO_3, as shown in Scheme 1b. Consequently, electrons will be transferred from WO_3 to RGO and the interface states, which finally results in the equilibrium of the Fermi levels of WO_3, RGO and the interface states. Under illumination, the Fermi level in WO_3 rises,[32] hence the photogenerated electrons can be transferred from WO_3 to RGO in WO_3–RGO, similar to TiO_2–RGO or CdS–RGO. The Schottky barrier formed in RGO and WO_3 would effectively hinder the electrons' backward transfer from RGO to WO_3, hence lowering the electron–hole recombination rate. The photogenerated electrons transferred from WO_3 to RGO will be transported to the substrate quickly to form an external circuit due to the remarkable charge carriers' mobility in RGO.[11]

As mentioned above, the presence of RGO reduces the recombination of the electron–hole by the Schottky barrier in WO_3–RGO. On the other hand, dopants or interfaces also act as active sites for the recombination of the electron–hole.[7] Therefore, RGO could play an unfavorable role as well. When the applied bias becomes more positive, a more effective electron–hole separation can be achieved by means of quick collection and transport of the photogenerated electrons by the RGO to the external circuit. As observed from the current work, when the applied bias exceeds 0.7 V *vs.* Ag/AgCl, RGO will mainly play a role of enhancing the charge transfer and reducing the recombination of the electron–hole, which results in higher photocurrent density over WO_3–RGO than that of WO_3. On the contrary, when lower bias is applied, RGO in WO_3–RGO will mainly play the unfavorable role of promoting the electron–hole recombination. Hence, the photocurrent density of WO_3–RGO is lower than that of WO_3 when the applied bias is less than 0.7 V *vs.* Ag/AgCl. This explanation agrees well with the observed LSV characteristics in Fig. 4.

Conclusions

In summary, we have reported, for the first time, the fabrication of a WO_3–RGO heterojunction photoanode, which shows enhanced photocatalytic performance for PEC overall water splitting at 1.0 V *vs.* Ag/AgCl under AM1.5 illumination, compared to the bare WO_3 electrode. This behavior can be explained by the effective separation and transport of photogenerated electron–hole by RGO with the help of interface states according to the Bardeen model. RGO does not only play a favorable role for the electron–hole separation by the efficient collection and transport of photogenerated electrons, but also serves as an active site for the recombination of electron–hole which is unfavorable for the electron–hole separation. A more positive applied bias is in favor of effective electron–hole separation by means of quick collection and transport of electrons by RGO. As a result, enhanced photocatalytic performance of WO_3 in the presence of RGO can only be obtained at a bias larger than 0.7 V *vs.* Ag/AgCl.

Notes and references

1 K. Maeda and K. Domen, *J. Phys. Chem. Lett.*, 2010, **1**, 2655.
2 A. Kudo and Y. Miseki, *Chem. Soc. Rev.*, 2009, **38**, 253.
3 X. B. Chen, S. H. Shen, L. J. Guo and S. S. Mao, *Chem. Rev.*, 2010, **110**, 6503.
4 K. Maeda, T. Ohno and K. Domen, *Chem. Sci.*, 2011, **2**, 1362.
5 K. Maeda, A. K. Xiong, T. Yoshinaga, T. Ikeda, N. Sakamoto, T. Hisatomi, M. Takashima, D. L. Lu, M. Kanehara, T. Setoyama, T. Teranishi and K. Domen, *Angew. Chem., Int. Ed.*, 2010, **49**, 4096.
6 J. S. Zhang, M. Grzelczak, Y. D. Hou, K. Maeda, K. Domen, X. Z. Fu, M. Antonietti and X. C. Wang, *Chem. Sci.*, 2012, **3**, 443.
7 S. Yan, Q. D. Huang, J. D. Lin, Y. Z. Yuan and D. W. Liao, *Acta Phys-Chim. Sin.*, 2011, **27**, 2406.
8 Y. Sasaki, H. Nemoto, K. Saito and A. Kudo, *J. Phys. Chem. C*, 2009, **113**, 17536.
9 T. T. Le, M. S. Akhtar, D. M. Park, J. C. Lee and O. B. Yang, *Appl. Catal., B*, 2012, **111–112**, 397.
10 Q. J. Xiang, J. G. Yu and M. Jaroniec, *Chem. Soc. Rev.*, 2012, **41**, 782.
11 K. I. Bolotin, K. J. Sikes, Z. Jiang, M. Klima, G. Fudenberg, J. Hone, P. Kim and H. L. Stormer, *Solid State Commun.*, 2008, **146**, 351.
12 X. Q. An and J. C. Yu, *RSC Adv.*, 2011, **1**, 1426.
13 W. Q. Fan, Q. H. Lai, Q. H. Zhang and Y. Wang, *J. Phys. Chem. C*, 2011, **115**, 10694.
14 Z. Y. Gao, N. Liu, D. P. Wu, W. G. Tao, F. Xu and K. Jiang, *Appl. Surf. Sci.*, 2012, **258**, 2473.
15 J. J. Guo, Y. Li, S. M. Zhu, Z. X. Chen, Q. L. Liu, D. Zhang, W. J. Moon and D. M. Song, *RSC Adv.*, 2012, **2**, 1356.
16 P. V. Kamat, *J. Phys. Chem. Lett.*, 2010, **1**, 520.
17 J. Zhang, J. G. Yu, M. Jaroniec and J. R. Gong, *Nano Lett.*, 2012, **12**, 4584.
18 Z. Ren, E. Kim, S. W. Pattinson, K. S. Subrahmanyam, C. N. R. Rao, A. K. Cheetham and D. Eder, *Chem. Sci.*, 2012, **3**, 209.

19 N. J. Bell, Y. H. Ng, A. J. Du, H. Coster, S. C. Smith and R. Amal, *J. Phys. Chem. C*, 2011, **115**, 6004.
20 Z. M. He, G. H. Guai, J. Liu, C. X. Guo, J. S. C. Loo, C. M. Li and T. T. Y. Tan, *Nanoscale*, 2011, **3**, 4613.
21 M. A. Butler, *J. Appl. Phys.*, 1977, **48**, 1914.
22 J. H. Kennedy and K. W. Frese, *J. Electrochem. Soc.*, 1978, **125**, 709.
23 P. Salvador, *J. Appl. Phys.*, 1984, **55**, 2977.
24 X. Liu, F. Y. Wang and Q. Wang, *Phys. Chem. Chem. Phys.*, 2012, **14**, 7894.
25 J. W. Qin, M. H. Cao, N. Li and C. W. Hu, *J. Mater. Chem.*, 2011, **21**, 17167.
26 X. Q. An, J. C. Yu, Y. Wang, Y. M. Hu, X. L. Yu and G. J. Zhang, *J. Mater. Chem.*, 2012, **22**, 8525.
27 O. Akhavan, M. Choobtashani and E. Ghaderi, *J. Phys. Chem. C*, 2012, **116**, 9653.
28 Y. H. Ng, A. Iwase, N. J. Bell, A. Kudo and R. Amal, *Catal. Today*, 2011, **164**, 353.
29 N. L. Yang, J. Zhai, D. Wang, Y. S. Chen and L. Jiang, *ACS Nano*, 2010, **4**, 887.
30 W. Z. Li, J. Li, X. Wang, J. Ma and Q. Y. Chen, *Int. J. Hydrogen Energy*, 2010, **35**, 13137.
31 K. Chang and W. X. Chen, *ACS Nano*, 2011, **5**, 4720.
32 A. J. Nozik and R. Memming, *J. Phys. Chem.*, 1996, **100**, 13061.
33 G. Eda, C. Mattevi, H. Yamaguchi, H. Kim and M. Chhowalla, *J. Phys. Chem. C*, 2009, **113**, 15768.
34 Y. Lin, K. Zhang, W. F. Chen, Y. D. Liu, Z. G. Geng, J. Zeng, N. Pan, L. F. Yan, X. P. Wang and J. G. Hou, *ACS Nano*, 2010, **4**, 3033.
35 S. X. Min and G. X. Lu, *J. Phys. Chem. C*, 2011, **115**, 13938.
36 J. A. Seabold and K. S. Choi, *Chem. Mater.*, 2011, **23**, 1105.
37 J. Bardeen, *Phys. Rev.*, 1947, **71**, 717.
38 K. Huang and N. Q. Han, Semiconductor physics fundamentals, Science Press, Beijing, China, 1979; pp 198–220.

